Automation in Construction 125 (2021) 103652

Contents lists available at ScienceDirect

Automation in Construction

journal homepage: www.elsevier.com/locate/autcon

Full-resolution 3D imaging for concrete structures with dual-polarization GPR

Kien Dinh [a,*], Nenad Gucunski [b], Khiem Tran [c], Alexandre Novo [d], Tu Nguyen [e]

[a] NDT Concrete LLC, Deltona, FL, USA
[b] Department of Civil & Environmental Engineering, Rutgers University, NJ, USA
[c] Department of Civil & Coastal Engineering, University of Florida, Gainesville, FL, USA
[d] IDS North America Inc., CO, USA
[e] Department of Civil, Construction, and Environmental Engineering, University of Alabama, AL, USA

ARTICLE INFO

Keywords:
GPR
Concrete
SAFT
3D imaging
Dual-polarization
Steel bar debonding
Concrete delamination

ABSTRACT

Ground-penetrating radar (GPR) is one of the most commonly used technologies for concrete inspection. This technology's main limitation is that its raw data are complex and only understood by GPR experts. Thus, this study's ultimate goal was to explore effective strategies for transforming GPR data collected by dual-polarization antennas into a more intuitive form of three-dimensional (3D) images. To understand the strategies' performance, they were implemented on a 1mx1m section of a reinforced concrete slab specimen. The evaluation of the results indicated a great benefit of the dual-polarization GPR system that created an accurate, high-resolution 3D representation of concrete with a single scanning direction dataset. More importantly, while there were differences between the 3D images obtained by different polarization, their combined use provided a comprehensive visualization of the concrete specimen's interior, which displayed reinforcements in two directions, steel bar debonding, and concrete delamination.

1. Introduction

Ground-penetrating radar (GPR) is a frequently used nondestructive evaluation (NDE) technology for civil engineering infrastructures [1]. With a very high speed of data collection, GPR can generate a large amount of data, which comprises a series of A-scans at discrete survey locations. Those A-scans can either be interpreted directly for layer-like structures such as pavements [2,3], or serve as the raw inputs for further data processing or image reconstruction [4]. For concrete structures, GPR has different applications. For example, it can help detect steel bars [5,6], estimate cover thickness for construction quality assurance/quality control [7,8], or to evaluate and monitor the deterioration progression of structural members [9–15].

Standard practice in concrete scanning with GPR involves the use of high-frequency antenna systems (typically from 1GHz to 3GHz) with HH polarization, i.e., antenna dipole being oriented orthogonal to the scanning direction. In such a system, the antenna box is connected to a control unit with a screen or a separate device (laptop or tablet) for real-time data visualization. While collecting data, the operator looks for the presence of rebar features on the screen and accordingly marks them on the structural element. Based on the operator's skills and the structure's complexity, this can be an easy task or an arduous endeavor, especially when other commonly found objects such as post-tension cables, conduits, radiant heating, etc., are also taken into consideration.

Concerning data processing/interpretation, a common practice is that a series of adjacent GPR profiles have to be simultaneously inspected to determine the position and size of a subsurface target [16]. As one can realize, such an inspection will be error-prone, time-consuming, and labor-intensive, considering that the analyst will have to go back and forth between B-scan images. Besides, while GPR signals/images may contain a vast amount of information, they are also very complex to analyze and not easy to understand by a GPR novice [17]. To be more specific, what one observes in a GPR profile usually does not indicate a subsurface object's true geometry and location. For instance, a hyperbola in the GPR profile is typically an indication of a point-like entity such as void, rebar, post-tensioning cable, etc. While the hyperbola's apex corresponds to the reflecting object's horizontal location, several data processing steps are still needed to obtain its correct depth.

* Corresponding author.
E-mail addresses: kien@ndt-concrete.com (K. Dinh), gucunski@soe.rutgers.edu (N. Gucunski), khiem.tran@essie.ufl.edu (K. Tran), alexandre.novo@idsgeoradar.com (A. Novo), nttu@crimson.ua.edu (T. Nguyen).

https://doi.org/10.1016/j.autcon.2021.103652
Received 5 July 2020; Received in revised form 1 February 2021; Accepted 26 February 2021
Available online 3 March 2021

All the above factors have led to the fact that the data collected by GPR technology are usually analyzed by experts in each corresponding application [17]. It has been observed that even experienced users may have difficulty analyzing raw GPR images. For example, a recent study [18] indicated that it would be challenging to detect concrete delamination below the top reinforcement (i.e., intermediate and deep delaminations) in B-scan images. The reasons include (1) the masking effect caused by top reinforcing bars and (2) the co-existence of multiple reflections near the slab's bottom. As another illustration of this problem, many studies focused on explaining the formation of GPR image signatures [19–23]. That is to say; there exists a need to have a practical and effective methodology for visualizing and analyzing GPR images. In line with previous studies [24–33], the main hypothesis herein is that full resolution, three-dimensional (3D) GPR imaging would help ease such data analysis/visualization problems.

That being said, the most recent study [16] suggested that 3D C-scans are increasingly popular as a GPR data visualization method. However, the authors of that study stated that "the process of generating C-scans is still immature, and yet to be standardized." Based on that, they developed a workflow for standardizing the process of creating 3D GPR images. While their workflow is appropriate for many GPR imaging problems, it was found to have the following limitations. First and foremost, as will be seen in the subsequent sections, an image created by that workflow only shows an approximation and not a true, full-resolution representation of subsurface objects. Second, for the data collected densely, the 3D image obtained with that workflow may contain reconstruction artifacts. Third, C-scans do not allow one to view the 3D volume from different perspectives. Fourth, one will have to scroll through different slices to inspect and fully understand the 3D image. Finally, it is not appropriate for the data collected by dual-polarization GPR system, as described in the next paragraph.

In recent years, some manufacturers have accommodated two antennas in a unique all-in-one dual-polarized GPR unit. Those two antennas are oriented perpendicular to each other in one plastic case (dual polarization) to capture more information for the same surveying effort. As in a conventional GPR system, one antenna is oriented orthogonal to the survey line, i.e., HH polarization, which is the most sensitive to longitudinal metal objects perpendicular to the scanning direction. The other one is oriented parallel to the survey line, i.e., VV polarization, which is the most receptive to the steel bars that lie alongside the scanning direction. So, in a single profile, data from both polarizations are gathered and displayed simultaneously, aiding in the real-time data interpretation and speeding up the whole scanning process.

Despite such a great benefit of dual-polarization GPR, there have been very few studies on the 3D visualization of the data collected by that system. Concerning concrete imaging application, one rare effort was made by Hugenschmidt et al. [31] when they compared three different strategies for obtaining 3D images of a retaining wall with a dual-polarization GPR dataset. To be specific, the three strategies that they used were (1) Two-dimensional (2D) migration of data from HH antenna only, (2) 3D migration followed by data fusion, and (3) 2D inverse scattering followed by interpolation and data fusion. However, while some promising results showed 3D images with rebar locations, they were based on a commercial GPR software with very complicated processing algorithms. For example, for the data fusion in the second strategy, the authors had to do the following steps. First, they decomposed the dataset from each antenna into five frequency ranges using wavelet transform. Then, they merged the two traces of each frequency range from the two datasets using a wavelet fusion algorithm. That was finally followed by the reconstruction of the fused traces using the inverse wavelet transform.

For other applications, a noticeable study concerning the use of full-resolution imaging for dual-polarization data was found in the area of geology [32]. In the study, Marchesini and Grasmueck investigated the impact of spatial sampling and antenna polarization on the 3D GPR imaging of subsurface fractures. The dual-polarization data was collected by surveying a limestone quarry in two perpendicular directions with the conventional HH antenna configuration. After comparing the quality of the images obtained by varying profile spacing and antenna polarization, they concluded that, for that specific problem, the acquisition of a single survey with a denser grid is a preferred approach rather than repeated surveys with different antenna polarization and increased profile spacing. One of the reasons the authors of the study did not recognize the benefit of dual-polarization GPR was because their problem did not involve polarization-dependent features such as steel reinforcing bars in concrete.

Considering everything stated above, this study's ultimate goal was to explore and understand various strategies for transforming data collected by a dual-polarization GPR system into a more intuitive form of 3D images. It is worth noting that, while the focus is on creating full-resolution 3D GPR images, the conventional method based on the interpolation of 2D slices is also included for comparison. Data collection on real concrete slab specimens aimed to verify the assumption that dual-polarization antennas would help eliminate the need to collect data in two perpendicular directions. In summary, this study aimed to answer whether one can create high-resolution 3D images of concrete, which show the objects/defects of interest, with a dataset from only one scanning direction. As will be seen in the subsequent sections, the method developed in this study will enable clear and more accurate visualization of the concrete interior with the data collected in such a manner.

2. Principles of GPR

GPR is a geophysical technology initially developed to explore subsurface configuration. As depicted in Fig. 1, commonly used GPR systems for concrete scanning or utility locating incorporate within its unit one or multiple antennae, a control unit, a hand-held cart, or a pushing wagon. As can be seen, the hand-held cart is more flexible in the sense that it can be used for a small working area/space and with any test orientation. However, the pushing wagon is more convenient for surveying a large horizontal surface such as a bridge deck, parking garage, construction field, or pavement. When the system is operated, the encoder in the cart or wagon helps determine the travel distance of the antenna based on the number of the wheel rotating cycles.

Concerning the data collection, at each scan location, the transmitting element of the antenna emits a short pulse of an electromagnetic wave. A part of the energy will go directly to the receiving element to form what is called a cross-talk, or a direct/air-wave. The remainder will go into the concrete or soil, and a portion of it will be reflected when the pulse reaches an interface between two media of contrasting dielectric constant. The strength (amplitude) of the reflected wave at the receiving antenna will be recorded by the system. A plot of the amplitude versus time for a scan location is an A-scan. A stack of many of those A-scans for a survey line will create an image, which is called a B-scan. As can be seen in Fig. 2, the time on the vertical axis of the B-scan indicates how long it takes for a signal to travel from the transmitting element of the antenna to a pixel location and then back to the receiving element. The horizontal axis indicates the traveling distance of the antenna.

Very importantly, GPR analysts should be aware of the following to interpret GPR image/signals effectively. First, the reflected waveforms in a raw GPR B-scan do not always indicate the object location. A small inclusion/object such as void or rebar will appear distortedly in the raw B-scan as a hyperbolic signature [4–7]. Second, the antenna's orientation/polarization will have a significant effect on what is observed in the GPR image. For instance, while longitudinal metal objects that lie in the direction of the antenna dipole will produce strong electromagnetic reflections, those perpendicular to the dipole will be much less visible in the resulting B-scan. Thus, a full understanding of what is hidden inside the concrete usually requires GPR data to be collected in perpendicular directions [30,31]. However, with a dual-polarization antenna, it is expected that the same can be achieved through surveying only in one

(a) (b)

Fig. 1. Commonly-used GPR systems for (a) concrete scanning and (b) utility locating.

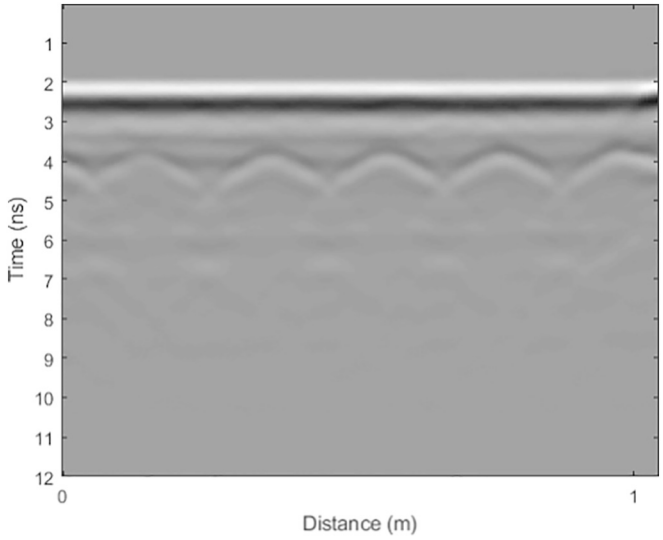

Fig. 2. Example of a raw B-scan.

direction. Besides, while the effect of antenna polarization has been well recognized, the authors of this study realized it had not been fully exploited for a concrete imaging application.

3. Data processing algorithms

Most GPR imaging applications' ultimate goal is to visualize/display reflecting objects at their correct locations. Since that is not the case in raw GPR image data, a migration usually needs to be performed to focus scattering energy to the true reflector's location. While there exist different methods for doing so [34], this study has selected the so-called synthetic aperture focusing technique (SAFT) for further investigation. The main reason was that this technique is easy to understand and implement. It has been used extensively to rebuild images from synthetic aperture radar (SAR) and ultrasonic phased array data [35–43]. Furthermore, it allows us to define a flexible imaging space whose dimensions and resolution do not depend on those of GPR B-scans. It is an essential factor when it comes to the step of image fusion when one would like to merge 3D images provided by different datasets.

Mathematically, the SAFT is based on the superposition of images obtained from projecting individual A-scans back into the evaluated/imaging region. Since A-scans are usually presented as time-domain signals, the technique may also be called time-domain back-projection [39]. Because the projection can be implemented in either two- or three-dimensional spaces, there are 2D- and 3D-SAFT algorithms, respectively. In the following, those two algorithms will be evaluated on the pretext of using a dual-polarization GPR antenna for a 3D concrete imaging application. As one may hypothesize, an image provided by the 3D-SAFT should be more accurate than the one obtained with the 2D-SAFT. The reason is, because of the cone-shaped nature of the GPR beam, a reflector/object observed on a B-scan may not necessarily lie in the same vertical plane as the antenna.

It should also be noted that the SAFT algorithms employed in this study belong to a class of techniques known as scalar migration. It is different from another class, the so-called vector migration, which accounts for the GPR antenna's radiation pattern [44]. To be more specific, the scalar migration methods assume that the GPR antenna is omnidirectional, which radiates equally in all directions. As such, when projecting A-scan back into the imaging region, two pixels/voxels of the same signal propagation time will be treated equally, i.e., being assigned the same amplitude value. On the other hand, as its name implies, the vector migration methods consider electromagnetic wavefields' vectorial character. Thus, it may apply different gain for pixels/voxels in different directions when performing an A-scan projection. Based on this idea, one may assume this migration technique will help eliminate the need to collect multi-polarization GPR data. A previous study has shown that it is only valid for imaging polarization-independent features [45].

Concerning 3D visualization, this study employs the volume rendering technique to display the SAFT algorithms' results. The 3D array of digital data is the most commonly used approach for visualizing 3D data in both medicine and nondestructive evaluation [46]. Its main idea is that each voxel's amplitude in the imaging space will represent the probability/density of a reflective surface being at that location. In other words, the higher the amplitude value a voxel has, the more likely a reflecting object exists at the corresponding location. When it comes to deciding which voxels represent a reflecting object, a specific but variable threshold will be chosen. Because of signal attenuation, a voxel representing a deeper object tends to have a smaller amplitude than those representing a shallower one, a gain function can be applied to compensate for such loss.

3.1. 2D-SAFT algorithm

The 2D-SAFT is a method in which A-scans are projected into the 2D slice that corresponds to the raw B-scan. Since the output of this method is a 2D image for each GPR survey line, interpolation will be needed to generate the desired 3D model. While the overall process for obtaining a 3D image using the 2D-SAFT technique is depicted in Fig. 3, each of the steps will be described in the following sub-sections.

3.1.1. Time-zero correction and background removal

In this first step, while the objective of time-zero correction is to move the zero time to the concrete surface location, the background removal is to eliminate the amplitudes associated with the direct-coupling reflection. Such removal is important as it enhances the visi-

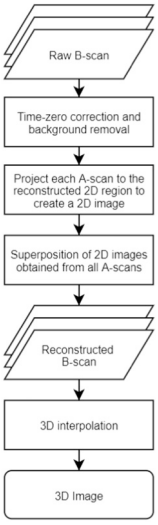

Fig. 3. Process for obtaining a 3D image based on the 2D-SAFT algorithm.

bility of objects below the concrete surface [4]. In terms of computation, while the time-zero location may vary between different ground-coupled antennae and should be calibrated for each application type, the background removal can be performed using the method of mean subtraction as shown in Eq. (1).

$$S^i_{br}(t) = S^i_{raw}(t) - \frac{\sum_{j=1}^{N} S^j_{raw}(t)}{N} \tag{1}$$

where

$S^i_{raw}(t)$: Signal amplitude of A-scan number i at time t.

$S^i_{br}(t)$: Signal amplitude of A-scan number i at time t after background removal.

N: Number of A-scans on the B-scan.

3.1.2. Project each A-scan into the reconstructed 2D region

In the second step, each A-scan in the time domain will be projected into the reconstructed 2D region. Specifically, for each A-scan, the algorithm first determines the transmitter and receiver locations. Then, based on an assumed or calibrated velocity of GPR signals, it will calculate the two-way travel time corresponding to each pixel/point in the 2D image/region. As defined in Eq. (2), the resulting travel time will be used to assign the projected amplitude for that pixel.

$$A^i_P = S^i_{br}\left(t = \frac{L^i_P}{V_{signal}}\right) \tag{2}$$

where

A^i_P: Amplitude of pixel P in the reconstructed 2D image obtained from A-scan number i.

$S^i_{br}(t)$: Signal amplitude of A-scan number i at time t.

L^i_P: Travel length from the transmitter to pixel P and back to the receiver, corresponding to A-scan number i.

V_{signal}: Assumed velocity of GPR signal.

3.1.3. Superposition of 2D images obtained from all A-scans

As with other migration techniques, the SAFT is also based on the principle of superposition. Specifically, the 2D images obtained from the previous step for individual A-scans are added up to get the reconstructed B-scan for each survey line. Eq. (3) explains the operation for each pixel.

$$A_P = \sum_{i=1}^{N} A^i_P \tag{3}$$

where

A_P: Aggregated amplitude of pixel P in the reconstructed 2D image.

N: Number of A-scans in the survey line (synthetic aperture).

3.1.4. Linear interpolation between 2D images

This step aims to obtain the missing information, i.e., the amplitudes for the voxels that lie in the spatial region between reconstructed B-scans. It is usually achieved using a technique known as interpolation. Although there exist different methods to interpolate data, linear interpolation is the most commonly used algorithm and, therefore, is adopted in this study. Specifically, with this method, the interpolated amplitude at a query point I is found using Eq. (4).

$$A_I = \frac{A_1 \times d_2 + A_2 \times d_1}{d_1 + d_2} \tag{4}$$

where

A_I:The amplitude value for the point I to be interpolated between two reconstructed 2D images.

A_1*and* A_2: The amplitude values of two pixels (I_1*and* I_2) on the two adjacent B-scans with the same horizontal and vertical coordinates as the point I.

d_1*and* d_2: The distances from point I to pixels I_1*and* I_2, respectively

3.2. 3D-SAFT algorithm

The 3D-SAFT is a method in which each A-scan in the entire data set is projected directly into the reconstructed 3D region. The outputs, i.e., 3D images of the same size, are then superimposed for all A-scans to obtain the final 3D image. While the 3D-SAFT algorithm's overall process is depicted in Fig. 4, each of the steps is described as follows.

3.2.1. Time-zero correction and background removal

This step is similar to the one described in the 2D-SAFT algorithm without any differences. Therefore, its description is not repeated in this section.

3.2.2. Project each A-scan into the reconstructed 3D region

This step reflects the main difference between the 2D-SAFT and the 3D-SAFT algorithm. Specifically, in the 3D-SAFT method, each A-scan is projected directly into the reconstructed 3D region, with the voxel amplitude defined by Eq. (5).

$$A^i_V = S^i_{br}\left(t = \frac{L^i_V}{V_{signal}}\right) \tag{5}$$

where

A^i_V: Amplitude of voxel V in the reconstructed 3D image obtained from A-scan number i.

$S^i_{br}(t)$: Signal amplitude of A-scan number i at time t.

L^i_V: Travel length from the transmitter to voxel V and back to the

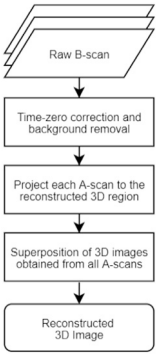

Fig. 4. Process for obtaining a 3D image based on the 3D-SAFT algorithm.

receiver, corresponding to A-scan number *i*.

V_{signal}: Assumed velocity of GPR signal.

As previously mentioned, this technique is more accurate than the 2D-SAFT because electromagnetic waves propagate in space in all directions. That is to say, a 3D migration of GPR data will reveal more accurately the reflecting object's location.

3.2.3. Superposition of 3D images obtained from all A-scans

Similar to the 2D-SAFT technique, the 3D images obtained from projecting individual A-scans in the previous step will be superimposed to achieve the desired 3D image. This operation is illustrated in Eq. (6) for each individual voxel.

$$A_V = \sum_{i=1}^{N} A_V^i \tag{6}$$

where

A_V: Aggregated amplitude of voxel V in the reconstructed 3D image.

N: Number of A-scans in the data set (3D synthetic aperture).

4. Experimental data collection

4.1. GRP equipment

This study employs the C-thrue, a compact 2-GHz GPR system for concrete scanning manufactured by IDS GeoRadar [47,48]. As can be seen in Fig. 5, the system has two antennas, named by the manufacturer as "shallow" or "HH," and "deep" or "VV." The antennas are oriented perpendicular to each other with a 10-cm spacing distance. The unit has a multi-touch screen for an embedded PC, an integrated control unit (DAD), and four wheels for distance measurement. In case one or more wheels do not rotate for some reason, the system will calculate the antenna position based on the wheel with the longest traveling distance. Since the unit can collect the data in both forward and backward directions while the two antennas are not located at the same position, a GPR analyst should take into account those two factors for a correct georeferencing.

Concerning the orientation, while the HH antenna has the dipole orthogonal to the scanning direction, the one of the VV antenna is parallel to that direction. It is worth noting that the names "shallow" and "deep" antennas above do not mean they have different signal frequencies. The VV antenna was named "deep" because, when it crosses on top of a transverse steel bar, its transmitted signal is reflected less by that bar than the one for the HH antenna. Consequently, more energy will continue to penetrate into the concrete.

4.2. Concrete slab specimens and data collection

As depicted in Fig. 6, three concrete slab specimens have been cast at the University of Florida in Gainesville, FL, USA, for this research. While two of them (Fig. 6a), with a varying concrete cover thickness, were used to calibrate the time-zero and the GPR signal's velocity, the third one (Fig. 6b, c & d) was of primary interest for 3D imaging validation. Like a typical reinforced concrete slab, this primary specimen has two layers of steel reinforcing bars laid in both directions. The specimen is 122 cm wide, 122 cm long, and 18 cm thick. Each reinforcement layer consists of 16 mm diameter rebars (bar #5) spaced at 178 mm in both longitudinal and transverse directions. Besides, the specimen included two types of simulated defects, namely steel bar debonding and concrete delamination. Specifically, as shown in Fig. 6b and c, steel bar debonding was created using a plastic wrap of increasing thickness for five locations in the middle of the slab. The thinnest plastic layer is 0.8 mm, while the thickest one is 4 mm. For delamination, four of them were made by foam and embedded within the slab specimen. They either had different dimensions or were placed at different depths. The detailed information for each of them is provided in Table 1.

Eight survey lines were set up for data collection for each specimen in Fig. 6a. As mentioned earlier, the purpose of B-scans collected from those survey lines was to calibrate the zero-time and GPR signals' velocity. Two survey grids were set up on the main concrete slab specimen, as shown in Fig. 6d. Specifically, the first grid had survey lines in both directions, parallel to the edges of the specimen. On the other hand, the second grid had survey lines in only one direction with an oblique angle of 45 degrees. The second grid's purpose was to evaluate the performance of 3D imaging strategies when data is collected in an arbitrary, unconventional direction. In this case, since both HH and VV antennas have an inclined angle of 45 degrees to steel reinforcing bars in both directions, it is expected that using data collected by any of those antennas for image reconstruction with 3D-SAFT will provide a similar result. For that same reason, it is not necessary to collect data in the perpendicular direction.

With respect to the resolution, the spacing between survey lines in each of the above grids is 1 cm. The reason for choosing that number was that it is smaller than the quarter-wavelength of GPR signal in concrete (about 1.13–1.67 cm for 2GHz antenna system), i.e., the criterion to be met for full-resolution 3D GPR imaging [33]. As illustrated in Fig. 7, four data sets were produced for the first survey grid, enabling multiple possible alternatives for 3D imaging and data fusion. For example, after using the 2D-SAFT or 3D-SAFT algorithm, one may choose to fuse two 3D images obtained from datasets 1 and 3. However, the other may want to merge those reconstructed from datasets 1 and 2, etc. While the former corresponds to what will need to be done with a conventional, single-component antenna, the latter precisely illustrates the benefit of using the dual-polarization GPR system. Finally, the antennas' data

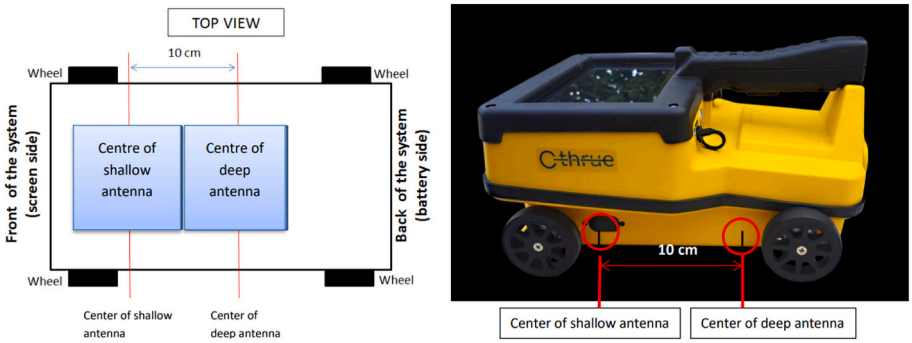

(a) C-thrue top view sketch (b) Dual polarization antenna positions

Fig. 5. IDS C-thrue GPR system [47].

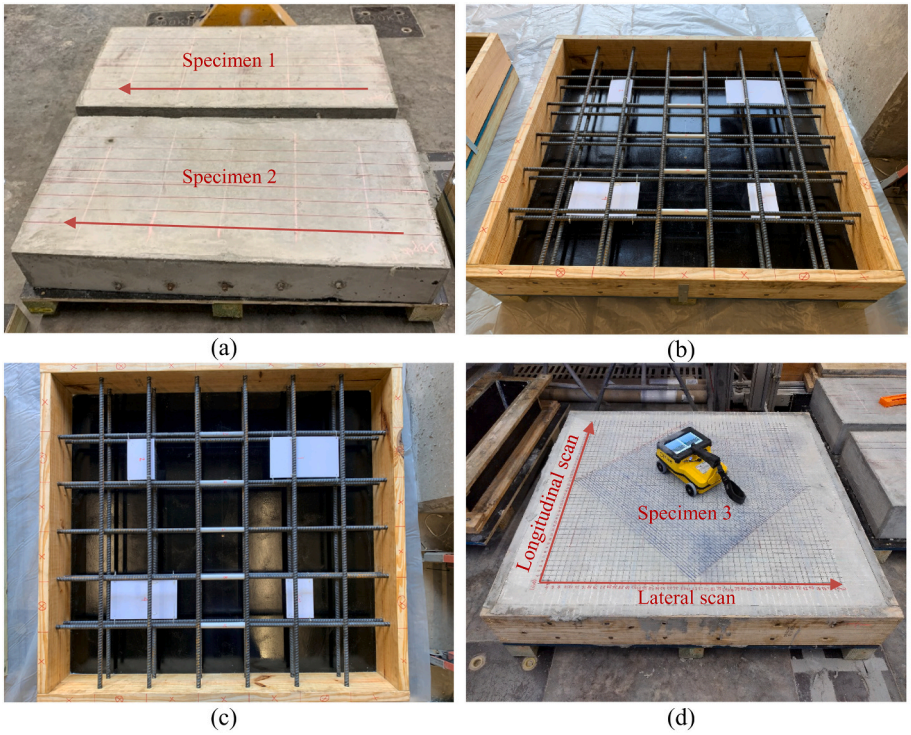

Fig. 6. Photos of concrete slab specimens.

Table 1
List of simulated delaminations.

#	Width (cm)	Length (cm)	Depth (cm)	Thickness (mm)
1	15.2	25.4	6.4	3
2	10.2	15.2	6.4	3
3	10.2	15.2	14	6
4	15.2	25.4	14	9

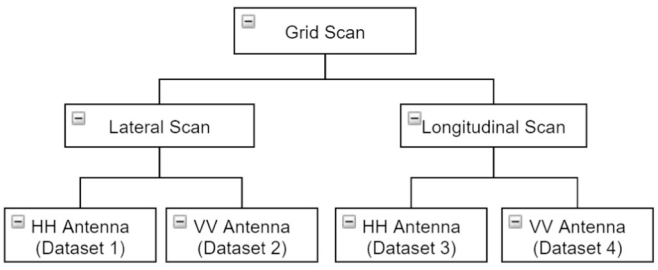

Fig. 7. Summary of data obtained for the first survey grid.

acquisition parameters were set at 5 A-scans per cm, a time window/range of 12 ns, and digitized to 512 samples per scan. GPR signals were collected without any gain or further filter being applied.

5. Results and discussion

Two MATLAB programs were developed in this study to implement the 2D-SAFT and 3D-SAFT algorithms automatically. As previously mentioned, the two essential parameters for those algorithms are the zero-time and the velocity of GPR signals. Since the specimens in this study were cast on the same date using the same concrete mixture, it is reasonable to assume the same signal velocity for those slabs. The calibration was a trial and error process when various zero-time and signal velocity were used in turn for B-scan image reconstruction. The final values of those parameters were determined by comparing the rebar depths (cover thicknesses) shown on reconstructed B-scans with the values measured directly on the specimens. While Fig. 8 shows the calibration's final results, the signal velocity was found to be equal to 0.093 m/ns. The zero-time was found to be located at 0.2 ns before the first positive peak of each A-scan. The calibrated velocity is slightly lower than a commonly used value of 0.1 m/ns because the concrete specimens were scanned when they were only 13 days old. In the following section, 3D images are generated for the main specimen (specimen 3) based on those calibrated values. They will be evaluated and compared to each other subjected to imaging strategy and/or antenna polarization. Since 3D images obtained with the 3D-SAFT algorithm are expected to be the most accurate representation of the test specimen, they will be presented and discussed first.

5.1. Results from the 3D-SAFT

Before evaluating the results, two issues concerning the computing time of the 3D-SAFT algorithm should be discussed. First, the selection of the size of each voxel for the imaging space will have a significant consequence on the total computing time of the 3D-SAFT. For example, when $1mm^3$ was selected as each voxel's size and 200 mm was selected as the depth of the 1 m × 1 m imaging area, it took 391,250 s to perform projection for all A-scans. However, if a cubic cell of $5mm^3$ was used instead as each voxel's size, computing time would be reduced 5^3 times to about 3130 s. Second, it was realized that the computing time could be further reduced if only some of the A-scans will be projected. In other words, if data was collected densely, one may choose to skip a certain number of A-scans when performing the back projection. For instance, the B-scans collected in this study has a density of 5 A-scans per cm. However, as previously mentioned, for full-resolution 3D GPR imaging, we only need the spacing between A-scan not greater than a quarter-wavelength. That means we can skip 4 A-scans in between those needed for image reconstruction. By doing so, we can further reduce the computing time for the above example to approximately 3130/5 = 626 s. That is also how the computing time was reduced in this research.

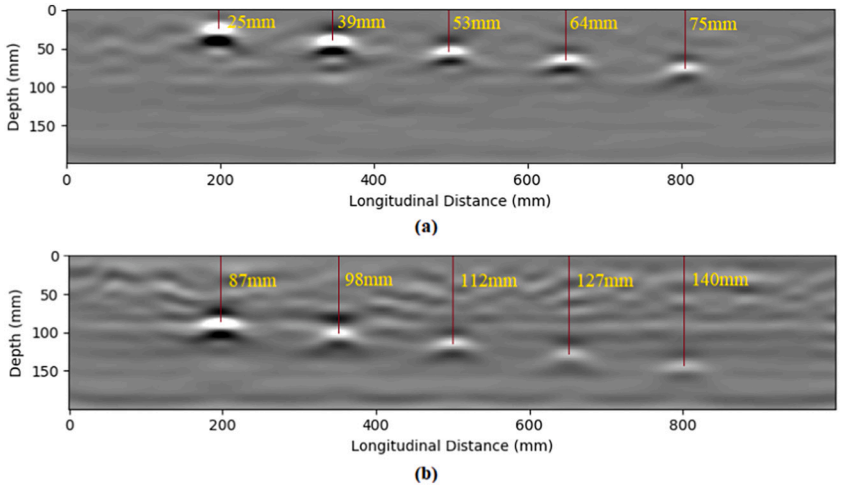

Fig. 8. Calibration of zero-time and signal velocity for (a) Specimen 1 and (b) Specimen 2.

5.2. 3D images obtained with the first survey grid

As presented in Fig. 9, the 3D images clearly show the objects and defects within the concrete specimen. These include steel reinforcing bars in two directions, steel bar debonding, shallow and deep concrete delamination. However, one can observe the similarities and differences between the images. Specifically, in terms of similarity, it is easy to recognize the repetition of information provided by datasets from the lateral (datasets 1 and 2) and longitudinal (datasets 3 and 4) scans. For example, while there is a slight difference in the color, 3D images obtained from both datasets 1 and 4 indicate the effects of debonding on steel bars' visibility. The reason is that those two datasets were obtained with the same antenna orientation/polarization. For convenience, the radiation direction/antenna dipole for each dataset was depicted in Fig. 9 as a two-headed red arrow.

With respect to the 3D images obtained by different antenna polarization, some interesting effects should be discussed as follows. First, while one can observe some differences in the visibility between transverse and longitudinal rebars in Fig. 9a and d, such differences almost disappear in Fig. 9b and c. The reason for that is the following. In the test specimen, the transverse/lateral bars are below the longitudinal direction ones. Therefore, due to an increase in cover thickness, the transverse bars' reflections will have smaller amplitudes than those from the longitudinal bars. While such a difference in amplitude will be increased when the antenna is oriented parallel to the longitudinal rebars, it will be decreased when the antenna is rotated 90 degrees to the position most reflective to the transverse rebars.

Second, while steel bar debonding effects are visible in Fig. 9a and d, they do not appear in Fig. 9b and c. Besides, a closer look at Fig. 9a and d clearly revealed the plastic wrap layer's effect. Specifically, the thicker this layer, the more it affects the visibility of the wrapped rebar. While this phenomenon is not yet fully examined in this study, it may be

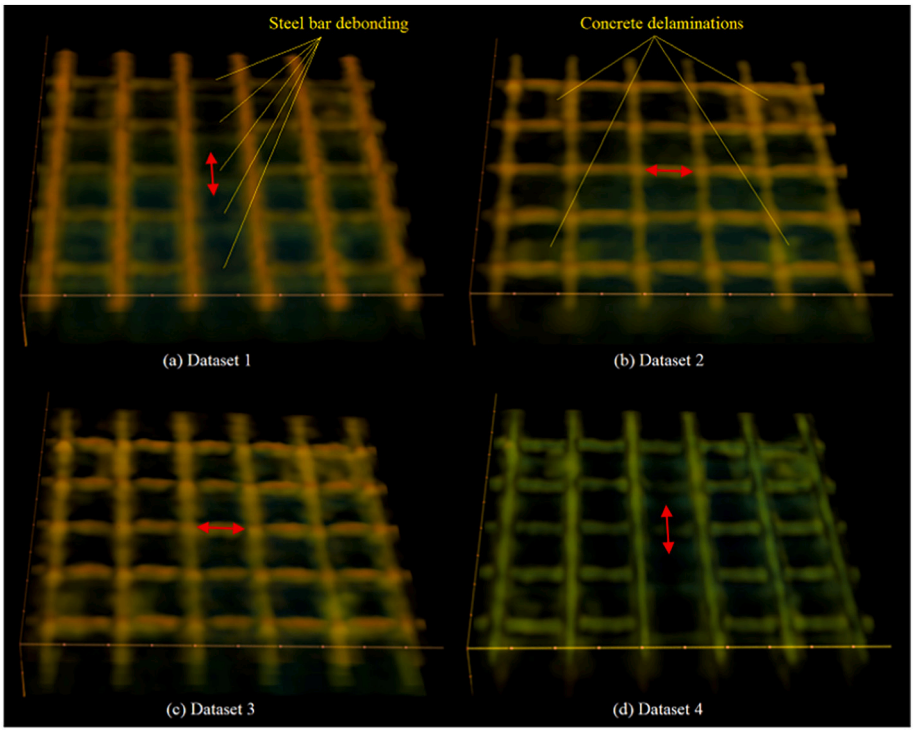

Fig. 9. 3D-SAFT imaging results for the first survey grid.

partially attributed to the effect of destructive interference. Two waveforms of reversed polarity may cancel out each other. This effect was explained in detail by Dinh and Gucunski [18] in their study of the effect of delamination thickness on the detectability of concrete delamination.

Regarding the current problem, it should be noted that there are three layers of material in the vicinity of steel bar/concrete debonding, namely concrete, air (i.e., plastic for the simulated debonding), and steel. Therefore, when a GPR signal propagates to this region, there will be two waveforms reflected. The first waveform is from the concrete/air interface and the second one is from the boundary of air/steel. In terms of polarity, while the first waveform will have the same polarity as the transmitted signal, the second waveform's polarity will be reversed. Thus, if the strengths of the two reflections are not much different, the sum of them will be close to zero. That was likely the case when the antenna was oriented perpendicular to the wrapped rebars. However, when the antenna was polarized parallel to the wrapped rebars, they became much more reflective and produced too strong reflections to be eliminated by the destructive interference.

Finally, the most important conclusion drawn from Fig. 9 is that GPR imaging with the 3D-SAFT helped visualize all the simulated concrete delamination clearly and accurately. This should be of particular interest to transportation agencies because the ability to detect concrete delamination in bridge decks and rigid pavements has been of high significance for many years. While a recent study has shown the great potential of GPR in detecting concrete delamination, it also pointed out the difficulties in detecting intermediate and deep delamination [18]. For illustration, Fig. 10 indicates how difficult it may be to identify directly concrete delamination on B-scan images. Specifically, there is almost no indication of delamination in these images, despite the fact that those were taken above the areas of simulated delaminations in specimen 3.

5.2.1. 3D images obtained with the second survey grid

As mentioned earlier, it was expected that the 3D-SAFT would have no problem reconstructing the data collected in an arbitrary, unconventional direction. Also, it was expected that the images obtained from HH and VV antenna data would look similar because the two antennas form an inclined angle of 45 degrees to steel reinforcing bars in both directions. Fig. 11 does confirm those expectations, although there are some differences in the color range between the two antennas' images. Such differences may be due to some detailed characteristics of each antenna. From the detection viewpoint, one can clearly see in both images steel bars in the two directions, some effect of steel bar/concrete debonding, shallow and deep delaminations. It should be noted again that the images in Fig. 11 were created from the data collected in only one direction.

5.2.2. Survey grid resolution and the 3D-SAFT

As has been seen, full-resolution 3D imaging offers excellent benefits compared to the conventional analysis of GPR B-scans. This method's only drawback is that it requires the data to be collected in a sufficiently dense survey grid. Although the quarter-wavelength criterion has already been established in the literature [33], the following experiment was conducted to understand it better for a concrete imaging application. Specifically, three different data resolutions (i.e., the spacing between A-scans in both directions) were selected to create 3D images with the 3D-SAFT algorithm. They were 1 cm, 2 cm, and 4 cm, respectively. The images obtained are shown in Fig. 12, along with a photo of the specimen for comparison. As can be realized, while we can only see some effect of the so-called *spatial aliasing* [33] in the image created with 2 cm spacing (Fig. 12c), that effect becomes evident for the image created with 4 cm spacing (Fig. 12d).

5.3. 3D images obtained with the 2D-SAFT

Similar to Fig. 9 in the previous section, Fig. 13 presents the results obtained with the 2D-SAFT for the datasets collected on the first survey grid. While these images generally indicate the locations of steel bars, the existence of steel bar debonding and concrete delaminations, in terms of quality, they are far not as good as the images created with the 3D-SAFT algorithm. In the images, one can easily observe reconstruction artifacts, which were the results of the 2D migration and interpolation performed between 2D images. For convenience, the orientation of the interpolation is depicted for each image in Fig. 13 by a yellow two-headed arrow. As a more detailed explanation, when an antenna runs parallel and very close to a rebar, we will see the reflections from that bar appear on the B-scan as a horizontal layer. When the interpolation is performed between those B-scans, it will create a longitudinal convex surface, rather than longitudinal rebar-like objects.

However, it is worth noting that the above does not mean the 2D-SAFT should not be used for GPR imaging applications. While the algorithm may not be appropriate for full-resolution 3D imaging, it will be of great use for many situations, some of which are as follows. First, as illustrated in Fig. 8, it can help us visualize the cross section of concrete below a survey line quickly. Second, it will be the only available alternative when the data is collected in a survey grid that does not meet the quarter-wavelength criterion for applying the 3D-SAFT. In many such cases, the obtained 3D images may look perfectly fine. Nevertheless, one should be aware that they are only an approximation, not an accurate representation of the surveyed elements.

5.4. Discussion

As described in many previous studies [4,16,20,29–31], 2D processing of B-scans and subsequent interpolation between survey lines has been the most common practice among GPR users to generate 3D GPR images. Such a process's popularity is up to the point that researchers even proposed a workflow to standardize it [16]. On the other

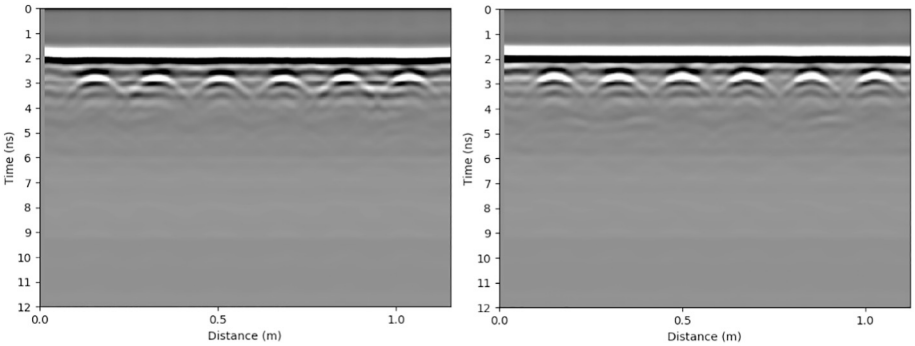

(a) B-scan with shallow delaminations (b) B-scan with deep delaminations

Fig. 10. Direct detection of delaminations on B-scan images.

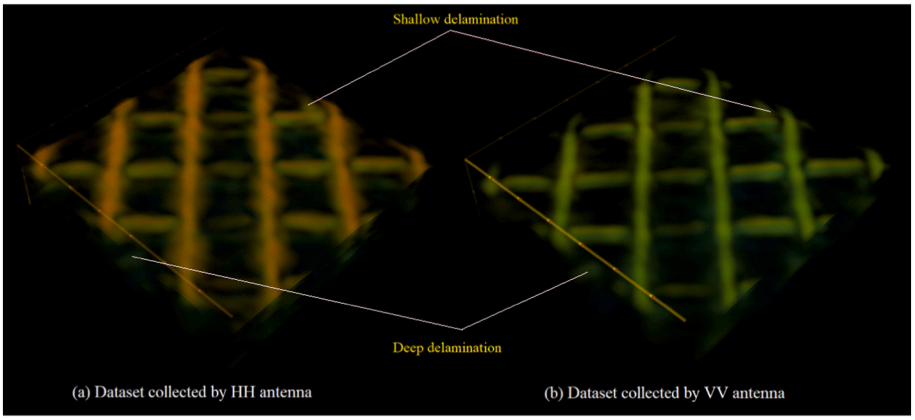

Fig. 11. Images obtained for the second survey grid with the 3D-SAFT.

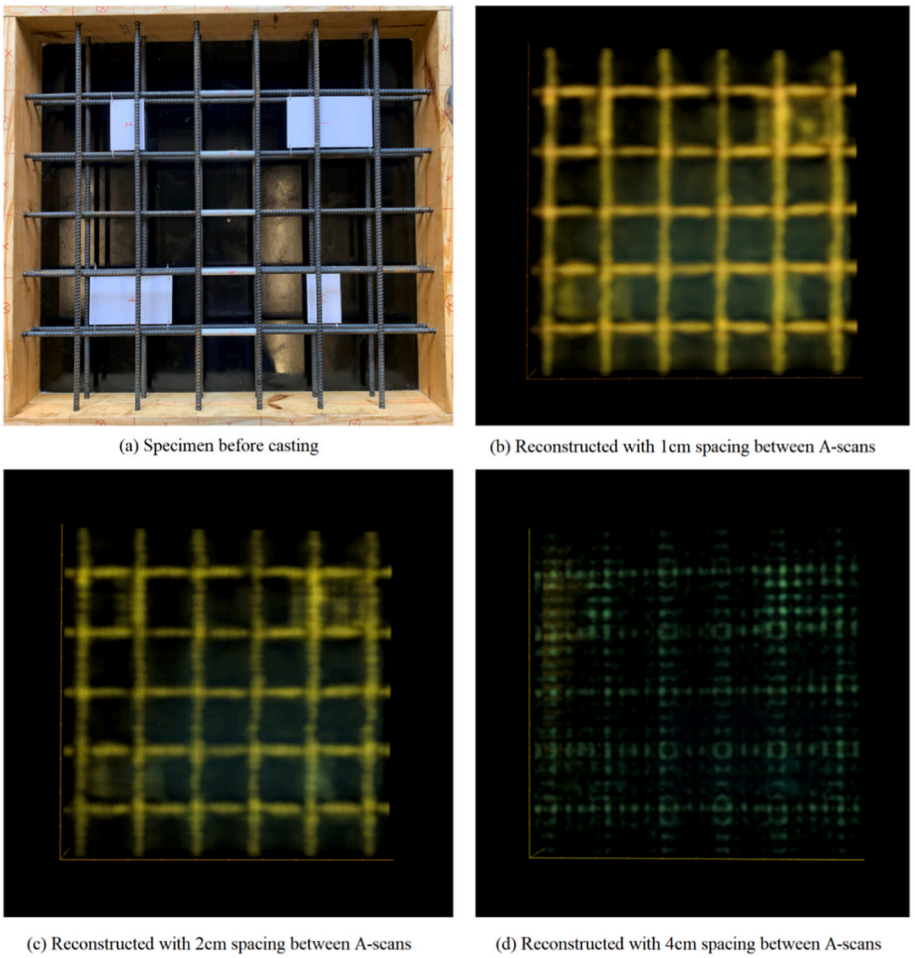

Fig. 12. 3D-SAFT based images for different grid resolution.

hand, very few studies realize or discuss its limitations, especially for data collected in a dense survey grid. This study has clearly demonstrated the drawback of the methodology employed in the current practice through the above implementation of two SAFT algorithms for a concrete slab specimen. As an alternative explanation for the aforementioned reconstruction artifacts, one can imagine that the 2D migration/SAFT does not take into account off-profile reflections, i.e., reflections from objects not lying directly below a survey line. According to [32], that will, consequently, lead to a false identification or erroneous interpretation of subsurface images.

As has been seen, while the 2D-SAFT described in this study also has the same problem as the above conventional method, the results from its 3D relative (3D-SAFT) showed great performance. First and foremost, the 3D-SAFT allowed the creation of full-resolution 3D images without introducing any reconstruction artifacts. Second, it allowed us to clearly visualize the interior of the concrete slab specimen with all the simulated defects. It is worth noting that previous studies have only demonstrated the 3D imaging algorithms for visualizing steel reinforcing bars in concrete structures. The current study is the first one that shows the capability of GPR in visualizing steel bars, steel bar

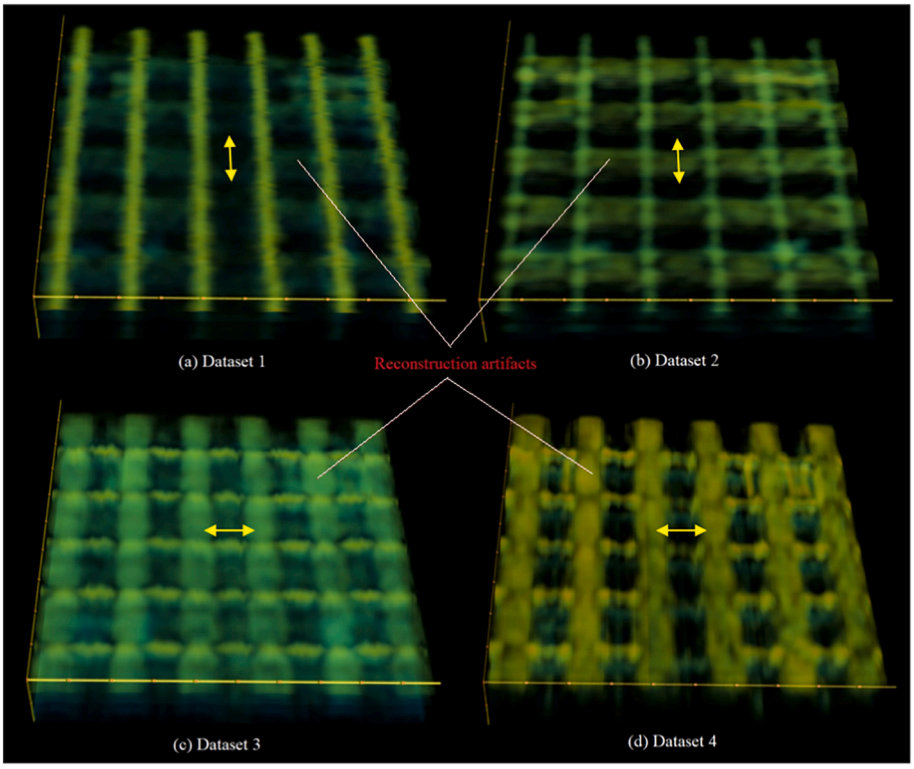

Fig. 13. 2D-SAFT imaging results for the first survey grid.

debonding, and concrete delaminations effectively. Those are the objects of extreme interest when inspecting or evaluating concrete structures. As such, both civil engineering researchers and GPR practitioners will benefit from the methodology described in this research.

6. Conclusions

GPR has been used extensively as a condition assessment and imaging technology for concrete structures. However, the conventional analysis of raw B-scans is complicated to new users and GPR experts. In addition, while a recent development of dual-polarization antenna may offer potential benefits, the antenna's complexity may be confusing to those familiar with a single antenna system only. In that context, this study was conducted to explore the use of a dual-polarization GPR system for a 3D concrete imaging application. Two algorithms based on the SAFT technique were used to reconstruct 3D images from various datasets collected with the dual-polarization antenna on a concrete specimen. The evaluation of the results led to the following conclusions. First, a great benefit of dual-polarization GPR systems is that they allow us to create full-resolution 3D images from the data collected in only one direction. Second and more important, such 3D images have demonstrated the capability of GPR in detecting different objects/defects, namely rebars in two directions, steel bar debonding, and concrete delamination. The main drawback of the methodology employed in this research is that it requires data to be collected in a dense survey grid with a sufficiently high geo-referencing precision. This study has shown that the methodology can be effectively implemented for the data collected manually. However, it will likely perform better in robotic data collection, which is also a continuation of this research.

Declaration of Competing Interest

The authors declare that they have no known competing financial interests or personal relationships that could have appeared to influence the work reported in this paper.

References

[1] J.H. Bungey, Sub-surface radar testing of concrete: a review, Constr. Build. Mater. 18 (1) (2004 Feb 1) 1–8, https://doi.org/10.1016/S0950-0618(03)00093-X.
[2] C. Le Bastard, V. Baltazart, Y. Wang, J. Saillard, Thin-pavement thickness estimation using GPR with high-resolution and superresolution methods, IEEE Trans. Geosci. Remote Sens. 45 (8) (2007) 2511–2519, https://doi.org/10.1109/TGRS.2007.900982.
[3] S. Lahouar, I.L. Al-Qadi, Automatic detection of multiple pavement layers from GPR data, NDT & E Int. 41 (2) (2008) 69–81, https://doi.org/10.1016/j.ndteint.2007.09.001.
[4] K. Dinh, N. Gucunski, T. Zayed, Automated visualization of concrete bridge deck condition from GPR data, NDT & E Int. 102 (2019 Mar 1) 120–128, https://doi.org/10.1016/j.ndteint.2018.11.015.
[5] K. Dinh, N. Gucunski, T.H. Duong, An algorithm for automatic localization and detection of rebars from GPR data of concrete bridge decks, Autom. Constr. 89 (2018 Feb) 292–298, https://doi.org/10.1016/j.autcon.2018.02.017.
[6] K. Dinh, N. Gucunski, T.H. Duong, Migration-based automated rebar picking for condition assessment of concrete bridge decks with ground penetrating radar, NDT & E Int. 98 (2018 Sep 1) 45–54, https://doi.org/10.1016/j.ndteint.2018.04.009.
[7] I. Al-Qadi, S. Lahouar, Portland cement concrete pavement: measuring rebar cover depth in rigid pavements with ground-penetrating radar. Transportation research record, J. Transp. Res. Board 1 (1907) (2005 Jan) 80–85, https://doi.org/10.3141/1907-09.
[8] M.I. Hasan, N. Yazdani, Ground penetrating radar utilization in exploring inadequate concrete covers in a new bridge deck, Case Stud. Construct. Mat. 1 (2014 Jan 1) 104–114, https://doi.org/10.1016/j.cscm.2014.04.003.
[9] K. Dinh, T. Zayed, F. Romero, A. Tarussov, Method for analyzing time-series GPR data of concrete bridge decks, J. Bridg. Eng. 20 (6) (2014), 04014086, https://doi.org/10.1061/(ASCE)BE.1943-5592.0000679.
[10] K. Dinh, T. Zayed, S. Moufti, A. Shami, A. Jabri, M. Abouhamad, T. Dawood, Clustering-based threshold model for condition assessment of concrete bridge decks with ground-penetrating radar. Transportation research record, J. Transp. Res. Board 1 (2522) (2015 Aug) 81–89, https://doi.org/10.3141/2522-08.
[11] K. Dinh, N. Gucunski, J. Kim, T.H. Duong, Understanding depth-amplitude effects in assessment of GPR data from concrete bridge decks, NDT & E Int. 83 (2016 Oct 31) 48–58, https://doi.org/10.1016/j.ndteint.2016.06.004.
[12] K. Dinh, N. Gucunski, J. Kim, T.H. Duong, Method for attenuation assessment of GPR data from concrete bridge decks, NDT & E Int. 92 (2017 Dec 1) 50–58, https://doi.org/10.1016/j.ndteint.2017.07.016.
[13] N. Gucunski, B. Pailes, J. Kim, H. Azari, K. Dinh, Capture and quantification of deterioration progression in concrete bridge decks through periodical NDE surveys, J. Infrastruct. Syst. 23 (1) (2016 Jun 17), B4016005, https://doi.org/10.1061/(ASCE)IS.1943-555X.0000321.

[14] K. Dinh, T. Zayed, GPR-based fuzzy model for bridge deck corrosiveness index, J. Perform. Constr. Facil. 30 (4) (2015 Jul 30), 04015069, https://doi.org/10.1061/(ASCE)CF.1943-5509.0000815.
[15] J. Kim, N. Gucunski, K. Dinh, Deterioration and predictive condition modeling of concrete bridge decks based on data from periodic NDE surveys, J. Infrastruct. Syst. 25 (2) (2019 Feb 28), 04019010, https://doi.org/10.1061/(ASCE)IS.1943-555X.0000483.
[16] T.X. Luo, W.W. Lai, R.K. Chang, D. Goodman, GPR imaging criteria, J. Appl. Geophys. 165 (2019) 37–48, https://doi.org/10.1016/j.jappgeo.2019.04.008.
[17] A. Tarussov, M. Vandry, A. De La Haza, Condition assessment of concrete structures using a new analysis method: ground-penetrating radar computer-assisted visual interpretation, Constr. Build. Mater. 38 (2013) 1246–1254, https://doi.org/10.1016/j.conbuildmat.2012.05.026.
[18] K. Dinh, N. Gucunski, Factors affecting the detectability of concrete delamination in GPR images, Constr. Build. Mater. (2020), 121837, https://doi.org/10.1016/j.conbuildmat.2020.121837.
[19] D.J. Daniels, Ground Penetrating Radar, John Wiley & Sons, Inc, 2005, https://doi.org/10.1002/0471654507.eme152.
[20] H. Liu, Z. Long, B. Tian, F. Han, G. Fang, Q.H. Liu, Two-dimensional reverse-time migration applied to GPR with a 3-D-to-2-D data conversion, IEEE J. Select. Top. Appl. Earth Observ. Remote Sens. 10 (10) (2017) 4313–4320, https://doi.org/10.1109/JSTARS.2017.2734098.
[21] W. Al-Nuaimy, Y. Huang, M. Nakhkash, M.T.C. Fang, V.T. Nguyen, A. Eriksen, Automatic detection of buried utilities and solid objects with GPR using neural networks and pattern recognition, J. Appl. Geophys. 43 (2) (2000) 157–165, https://doi.org/10.1016/S0926-9851(99)00055-5.
[22] P. Gamba, S. Lossani, Neural detection of pipe signatures in ground penetrating radar images, IEEE Trans. Geosci. Remote Sens. 38 (2) (2000) 790–797, https://doi.org/10.1109/36.842008.
[23] E. Pasolli, F. Melgani, M. Donelli, Automatic analysis of GPR images: a pattern recognition approach, IEEE Trans. Geosci. Remote Sens. 47 (7) (2009) 2206–2217, https://doi.org/10.1109/TGRS.2009.2012701.
[24] U. Boeniger, J. Tronicke, Improving the interpretability of 3D GPR data using target–specific attributes: application to tomb detection, J. Archaeol. Sci. 37 (2) (2010) 360–367, https://doi.org/10.1016/j.jas.2009.09.049.
[25] J. Leckebusch, Ground-penetrating radar: a modern three-dimensional prospection method, Archaeol. Prospect. 10 (4) (2003) 213–240, https://doi.org/10.1002/arp.211.
[26] J. Leckebusch, R. Peikert, Investigating the true resolution and three-dimensional capabilities of ground-penetrating radar data in archaeological surveys: measurements in a sand box, Archaeol. Prospect. 8 (1) (2001) 29–40, https://doi.org/10.1002/1099-0763(200103)8:1<29::AID-ARP154>3.0.CO;2-T.
[27] L. Topczewski, F.M. Fernandes, P.J. Cruz, P.B. Lourenço, Practical implications of GPR investigation using 3D data reconstruction and transmission tomography, J. Build. Apprais. 3 (1) (2007) 59–76, https://doi.org/10.1057/palgrave.jba.2950060.
[28] L. Nuzzo, G. Leucci, S. Negri, M.T. Carrozzo, T. Quarta, Application of 3D visualization techniques in the analysis of GPR data for archaeology, Ann. Geophys. 45 (2) (2002) 321–337.
[29] C. Kohl, M. Krause, C. Maierhofer, J. Wöstmann, 2D-and 3D-visualisation of NDT-data using data fusion technique, Mater. Struct. 38 (9) (2005 Nov 1) 817–826, https://doi.org/10.1007/BF02481654.
[30] J. Hugenschmidt, A. Kalogeropoulos, The inspection of retaining walls using GPR, J. Appl. Geophys. 67 (4) (2009 Apr 1) 335–344, https://doi.org/10.1016/j.jappgeo.2008.09.001.
[31] J. Hugenschmidt, A. Kalogeropoulos, F. Soldovieri, G. Prisco, Processing strategies for high-resolution GPR concrete inspections, NDT & E Int. 43 (4) (2010 Jun 1) 334–342, https://doi.org/10.1016/j.ndteint.2010.02.002.
[32] P. Marchesini, M. Grasmueck, Impact of spatial sampling and antenna polarization on 3D GPR fracture detection, in: Proceedings of the XIII International Conference on Ground Penetrating Radar 2010 Jun 21, IEEE, 2020, pp. 1–6, https://doi.org/10.1109/ICGPR.2010.5550193.
[33] M. Grasmueck, R. Weger, H. Horstmeyer, Full-resolution 3D GPR imaging, Geophysics 70 (1) (2005) K12–K19, https://doi.org/10.1190/1.1852780.
[34] C. Özdemir, Ş. Demirci, E. Yiğit, B. Yilmaz, A review on migration methods in B-scan ground penetrating radar imaging, Math. Probl. Eng. 2014 (2014), https://doi.org/10.1155/2014/280738.
[35] J.C. Curlander, R.N. McDonough, Synthetic Aperture Radar, Wiley, New York, 1991.
[36] R. Bamler, P. Hartl, Synthetic aperture radar interferometry, Inverse Probl. 14 (4) (1998) R1.
[37] G. Franceschetti, R. Lanari, Synthetic Aperture Radar Processing, CRC Press, 1999.
[38] P.A. Rosen, S. Hensley, I.R. Joughin, F.K. Li, S.N. Madsen, E. Rodriguez, R. M. Goldstein, Synthetic aperture radar interferometry, Proc. IEEE 88 (3) (2000) 333–382, https://doi.org/10.1109/5.838084.
[39] O. Frey, E.H. Meier, D.R. Nüesch, Processing SAR data of rugged terrain by time-domain back-projection, in: SAR Image Analysis, Modeling, and Techniques VII. International Society for Optics and Photonics, 2005, p. 598007.
[40] K.J. Langenberg, M. Berger, T. Kreutter, K. Mayer, V. Schmitz, Synthetic aperture focusing technique signal processing, NDT Int. 19 (3) (1986) 177–189, https://doi.org/10.1016/0308-9126(86)90107-0.
[41] M. Spies, H. Rieder, Synthetic aperture focusing of ultrasonic inspection data to enhance the probability of detection of defects in strongly attenuating materials, NDT E Int. 43 (5) (2010) 425–431, https://doi.org/10.1016/j.ndteint.2010.04.002.
[42] M. Spies, H. Rieder, A. Dillhöfer, V. Schmitz, W. Müller, Synthetic aperture focusing and time-of-flight diffraction ultrasonic imaging—past and present, J. Nondestruct. Eval. 31 (2012) 310–323, https://doi.org/10.1007/s10921-012-0150-z.
[43] M. Schickert, M. Krause, W. Müller, Ultrasonic imaging of concrete elements using reconstruction by synthetic aperture focusing technique, J. Mater. Civ. Eng. 15 (2003) 235–246, https://doi.org/10.1061/(ASCE)0899-1561(2003)15:3(235).
[44] R. Streich, J. Van der Kruk, Accurate imaging of multicomponent GPR data based on exact radiation patterns, IEEE Trans. Geosci. Remote Sens. 45 (1) (2006) 93–103, https://doi.org/10.1109/TGRS.2006.883459.
[45] R. Streich, J. Van der Kruk, A.G. Green, Vector-migration of standard copolarized 3D GPR data, Geophysics 72 (5) (2007) J65–J75, https://doi.org/10.1190/1.2766466.
[46] R.A. Drebin, L. Carpenter, P. Hanrahan, Volume rendering, in: ACM Siggraph Computer Graphics 1988 Aug 1; Vol. 22, No. 4, ACM, 2020, pp. 65–74, https://doi.org/10.1145/378456.378484.
[47] IDS Georadar, C-Thrue User Manual: All-in-One Ground Penetrating Radar (GPR) for Accurate Scanning and Real Time Analysis, 2017.
[48] D. Pasculli, A. Natali, W. Salvatore, F. Morelli, D. Morandi, Investigation of reinforced concrete bridges by using a dual-polarized high-frequency GPR, in: Proceedings of the 2018 17th International Conference on Ground Penetrating Radar (GPR), Rapperswil, Switzerland, 18–21 June 2018, https://doi.org/10.1109/ICGPR.2018.8441633.